Extreme Mechanics Letters 15 (2017) 130–138

Contents lists available at ScienceDirect

Extreme Mechanics Letters

journal homepage: www.elsevier.com/locate/eml

Effects of surface tension on the suction forces generated by miniature craters

Liu Wang [a], Shutao Qiao [a], Nanshu Lu [a,b,c,*]

[a] Center for Mechanics of Solids, Structures and Materials, Department of Aerospace Engineering and Engineering Mechanics, The University of Texas at Austin, Austin, TX 78712, United States
[b] Department of Biomedical Engineering, The University of Texas at Austin, Austin, TX 78712, United States
[c] Texas Materials Institute, The University of Texas at Austin, Austin, TX 78712, United States

ARTICLE INFO

Article history:
Received 28 June 2017
Accepted 18 July 2017
Available online 27 July 2017

Keywords:
Craters
Surface tension
Elasto-capillary
Suction force
Reversible adhesive

ABSTRACT

There are emerging demonstrations that micro- or nano-craters engineered on polymer surfaces can enable enhanced adhesion. In the past, we have developed a framework for quantifying the suction forces produced by isolated macroscopic craters neglecting surface effects. In this paper, we take surface tension into consideration because it plays a significant role in miniature craters on soft polymers. We have derived linear and nonlinear elastic solutions for the elasto-capillary distortion in miniature hemispherical craters when they are demolded from the template. By implementing a user-element subroutine in finite element modeling (FEM) software ABAQUS, we have also simulated the demolding, compression, and unloading processes of the craters subjected to surface tension under large deformation. With the simulated volume changes of the crater, pressure drop and suction force can be deduced. We find that surface tension induced crater contraction has a negative effect on the generation of suction forces. We discover that reinforcing the crater surface by a thin and stiff shell can help sustain the crater shape after demolding. The effects of shell thickness and stiffness are quantitatively investigated through FEM and optimal parametric combinations are identified.

1. Introduction

Removable dry adhesives are designed to form a temporary bond without any liquid glue and ideally can be removed without damaging the adherend or leaving any residue on the adherend. Removable adhesives are used for wound care dressings, athletic tapes, surface protection films, note papers, and many other applications. Some removable adhesives are designed to be used multiple times. Removable adhesives generally have low adhesion and hence cannot support much load. Those capable of strong bonding can further enable reusable wall-mounted hangers, wall-climbing robots [1–3], wafer manipulators for micro-fabrication [4,5] as well as reliable but releasable tissue adhesives [6–10]. So far, gecko inspired micro-fibrils are probably the best examples of engineered removable dry adhesives which are strong for bonding but are easy to peel off when release is required [11–17].

In addition to extruding fibrils, removable dry adhesives can also be engineered by concavity. Suction is an attractive mechanism for attachment because it can combine high strength and quick release. In fact, macroscopic suction cups have been used ubiquitously as reversible adhesives in both nature and civilization. In nature, cephalopods such as octopus can manipulate items and reversibly anchor to rocks for prolonged time through negative pressure generated by mm-sized suction cups distributed over their arms [18–21]. Commercially, cm-sized suction cup hooks and electrocardiogram (ECG) electrodes are widely available. In robotics research, Kim et al. installed 60-mm-diameter suction pads on the tracked wheels of a wall-climbing robot which achieved an excellent climbing performance on a rough wall [2]. Analytical modeling and experimental evaluation of thin-walled suction cups have been conducted [22,23]. In addition, reusable adhesives have also been fabricated by combining concave shapes with fibrillary structures [9,24,25].

A simple alternative to such reusable adhesives are cratered surfaces where micro- or nano-scale dimples are engineered on polymer sheets [4,5,26,27]. For example, in 2014, Chang et al. created an array of submicron-surface craters on UV resin and measured adhesive shear strength on silicon wafer to be as high as 750 kPa [4]. In 2015, Choi et al. created an array of 1-μm-diameter craters on the surface of a multilayer polydimethylsiloxane (PDMS) and measured the adhesive shear strength to be 1.6 kPa, which exceeds the adhesive strength of the same PDMS with both flat surfaces and surface pillars [28]. Also in 2015, Akerboom et al. fabricated close-packed nano-dimples on 10:1 PDMS and

* Correspondence to: 512-471-4208, 210 E. 24th St, Austin, TX 78712, United States.
E-mail address: nanshulu@utexas.edu (N. Lu).

http://dx.doi.org/10.1016/j.eml.2017.07.004
2352-4316/

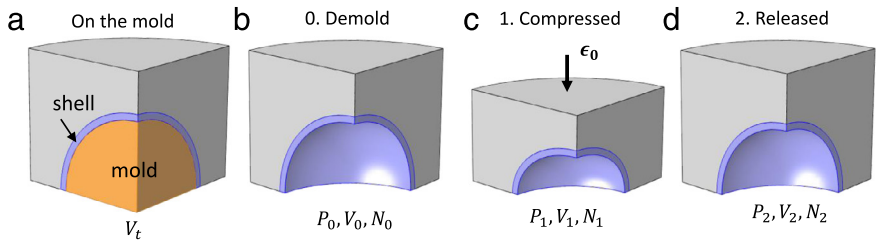

Fig. 1. Schematics for the deformation process of an isolated hemi-spherical crater with reinforcing shell. (a) Crater on the mold whose volume is defined by the molding template, V_t; (b) State 0: after demolding, the crater volume contracts to V_0 merely due to surface tension. (c) State 1: preload ϵ_0 is applied on the specimen to squeeze the crater to volume V_1; (d) State 2: crater volume recovers to V_2 after unloading.

found that the pull-off force is enhanced compared with flat PDMS control and that the pull-off force depends on the preload [29]. Most recently, Baik et al. fabricated microscale craters with dome-shaped protuberances inspired by octopus suction cups and their suction force measured under both dry and wet conditions turn out to be much larger than their pillared counterparts [30]. Pressure-sensitive adhesives are especially useful for applications where adhesion should only be activated whenever needed. Active miniature craters are proposed by Lee et al. in 2017 [5]. By coating a thermoresponsive polymer layer over a PDMS full of μm-sized craters, temperature-induced volume change of the craters can activate and deactivate suction and adhesion, without any externally applied forces [5].

Commonly used fabrication method for miniature craters is molding. The molding templates are created using either micromachining [28] or colloidal lithography [4,29]. Such methods worked well for UV resin [4] whose modulus is in the GPa range and 10:1 PDMS [29] whose modulus is in the MPa range. However, when researchers tried to mold 40:1 PDMS (shear modulus $\mu = 52$ kPa) with μm-sized craters, they found that after peeling off PDMS from the template, i.e. demolding, the craters in PDMS appeared to be much smaller than the domes on the molding template. After coating stiffer PDMS layers on the template before molding 40:1 PDMS, the craters were able to preserve the template shape very well after demolding [28]. We attribute the self-collapse of miniature craters on soft polymers after demolding to the so-called elasto-capillary phenomena [26,27].

To elaborate on how the elasto-capillary phenomena can affect the miniature craters, let us consider a crater of radius r in a polymer whose shear modulus is μ and surface energy density is γ. If constant surface energy density is assumed, surface tension would equal to surface energy density γ [31]. Since the total surface energy scales as γr^2 while the volumetric strain energy scales as μr^3, we can define a dimensionless elasto-capillary number

$$\eta = \gamma/(\mu r) \tag{1}$$

to represent the ratio of surface energy to strain energy. When the polymer is very stiff (μ is large) and/or the crater is very big (r is large), η would approach zero, which means the surface energy would be negligible compared with the elastic strain energy and therefore the crater cannot be deformed by surface tension. However, when the polymer is ultra-soft (μ is small) and when the crater is in micro- or nano-scale (r is small), η can be so large that the effects of surface tension is no longer negligible. In this case, the crater will try to reduce the surface energy (or surface area) through mechanical deformation. Experimentally, such elasto-capillary phenomena have been widely reported when η is near 1 [26,27,32,33]. Specific to craters, let us consider the experiments carried out by Choi et al. [28] where they tried to mold μm-sized craters out of 40:1 PDMS whose $\mu = 52$ kPa, $\gamma = 20$ mN/m [34,35], and $r \sim 0.5$ μm. Plugging into Eq. (1), we find $\eta = 0.769$, which suggests that due to surface tension, the crater may shrink significantly to reduce its surface area after demolding. Adding a stiff reinforcing shell to the crater proved to be an effective way to sustain the crater shape [28]. However, a quantitative characterization of the effects of surface tension and reinforcing shell on the suction force generated by those craters is still missing.

Following a framework developed for isolated macroscopic craters neglecting surface effects [36], here we analyze isolated hemi-spherical craters with reinforcing shells subjected to surface tension. The process of suction generation is illustrated using a quarter of the crater in Fig. 1. When the specimen is just cured and still on the molding template (Fig. 1(a)), the volume of the crater is denoted by V_t (Fig. 1(a)). After demolding, the crater contracts due to surface tension (Stage 0). At the end of Stage 0, the air inside the crater is the same as the ambient air so it is characterized by pressure P_0, volume V_0, and number of molecules N_0 (State 0, Fig. 1(b)). The suction effect is then realized in the following two stages:

1. Stage 1: the specimen is compressed by a nominal strain of ϵ_0, named the preload, against a flat plate (not shown in Fig. 1(c)), such that air is squeezed out of the crater. At the end of this stage, the remaining air in the carter is characterized by the triplet (P_1, V_1, N_1) (State 1, Fig. 1(c)).
2. Stage 2: the specimen is unloaded and the crater springs back. This action results in a pressure drop inside the crater which produces the suction force. At the end of this stage, the air in the crater is characterized by the triplet (P_2, V_2, N_2) (State 2, Fig. 1(d)). Accordingly, the pressure drop is

$$-\Delta P = P_1 - P_2$$

and the suction force is

$$F = -\Delta P A_2 \tag{2}$$

where A_2 is the projected area of the crater at State 2.

Key assumptions adopted in this paper are:

1. The air flows freely out of the crater upon loading (Stage 1), so that $P_1 = P_0$.
2. No air exchange takes place upon unloading (Stage 2), so that $N_2 = N_1$.
3. The entire process is isothermal and the air is an ideal gas, so that $P_1 V_1 = P_2 V_2$.

As a result, the pressure drop can be related to the crater volumes as

$$-\Delta P = \left(1 - \frac{V_1}{V_2}\right) P_0. \tag{3}$$

Therefore, the suction force becomes

$$F = \left(1 - \frac{V_1}{V_2}\right) P_0 A_2. \tag{4}$$

In this paper, we will quantitatively characterize the effects of surface tension and reinforcing shell on crater performance. Linear

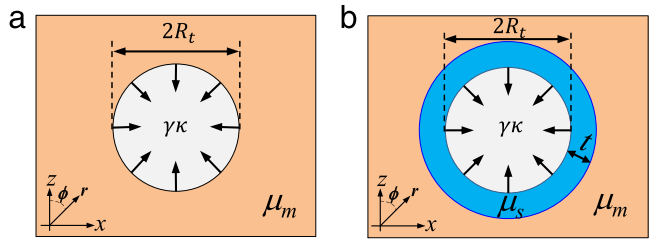

Fig. 2. Effective boundary value problems for Stage 0. (a) A spherical cavity of radius R_t inside a matrix of shear modulus μ_m. (b) A reinforcing shell of thickness t and modulus μ_s is added. Both the matrix and the reinforcing shell are assumed to be incompressible Neo-Hookean materials.

and nonlinear elastic formulation for Stage 0 and nonlinear elastic finite element modeling (FEM) of all three stages are described in Section 2. Analytical and FEM results are presented in Section 3. Concluding remarks are offered in Section 4.

2. Methods

2.1. Linear elasticity solutions for Stage 0

Given the axisymmetry of the specimen, this problem can be analyzed as a 2-D problem. By neglecting the interfacial shear stress between the specimen and the flat plate and by overlooking the surface tension effects at the rim of the crater, the hemi-spherical crater can be mirrored to a spherical cavity embedded in a polymer matrix (Fig. 2(a)). The matrix dimension is assumed to be much larger than the cavity size such that the matrix can be treated as infinitely large. The initial radius of the crater is R_t (as defined by the molding template shown in Fig. 1(a)) and the shear modulus of the polymer matrix is μ_m. Surface tension can be interpreted as a normal traction applied on the surface of the spherical cavity [37–39]:

$$t_n = \gamma\kappa \tag{5}$$

where κ is the sum of the two principal curvatures, which equals to $2/R_t$ initially.

We first solve the problem using linear elasticity in a polar coordinates defined in Fig. 2(a) by adopting Lur'e solution [40]. The displacement and stress fields can be expressed as

$$\begin{aligned} U_r &= Fr + \frac{G}{r^2} + P_2(\cos\phi) \\ &\quad \times \left[12A\nu r^3 + 2Br + 2C\tfrac{5-4\nu}{r^2} - 3\tfrac{D}{r^4}\right] \\ U_\phi &= \frac{dP_2(\cos\phi)}{d\phi} \times \left[(7-4\nu)\,A\,r^3 + Br + 2C\frac{1-2\nu}{r^2} + \frac{D}{r^4}\right] \end{aligned} \tag{6}$$

$$\begin{aligned} \frac{\sigma_{rr}}{2\mu_m} &= \left[2B - \frac{2C}{r^3}(10-2\nu) + \frac{12D}{r^5}\right] P_2(\cos\phi) \\ &\quad + \frac{F(1+\nu)}{1-2\nu} - \frac{2G}{r^3} \\ \frac{\sigma_{r\phi}}{2\mu_m} &= \left[B + \frac{2C}{r^3}(1+\nu) - 4\frac{D}{r^5}\right] \frac{dP_2(\cos\phi)}{d\phi} \end{aligned} \tag{7}$$

where U_r and U_ϕ are the displacements of cavity surface in the radial and hoop directions, respectively, and σ_{rr} and $\sigma_{r\phi}$ are the normal and shear stresses, respectively. $P_2(\cos\phi) = 1/2\left(3\cos^2\phi - 1\right)$ is the Legendre Polynomial of order two and ν is the Poisson's ratio of the polymer matrix. Coefficients A through G are to be determined by boundary conditions. The boundary conditions of Fig. 2(a) can be expressed as: in the far field, $\epsilon_{rr}^{\infty} = 0$; at $r = R_t, \sigma_{rr} = 2\gamma/R_t, \sigma_{r\phi} = 0$. Hence the only nonzero coefficient is found to be $G = -R_t^2\gamma/(2\mu_m)$, which gives the radial displacement of the crater surface $U_r = -R_t\eta/2$, where $\eta = \gamma/(\mu_m R_t)$ is the dimensionless elasto-capillary number. Therefore, at the end of Stage 0 (i.e. demolding), the hemi-spherical crater will deform to another hemi-sphere with a new radius of

$$R_0 = R_t\left(1 - \frac{\eta}{2}\right). \tag{8}$$

Eq. (8) shows that the change of crater radius $\Delta R = R_0 - R_t$ is linearly proportional to the elasto-capillary number η.

Lur'e formulism, i.e. Eqs. (6)–(7), can also be applied to solve a spherical cavity with a reinforcing shell subjected to surface tension, as depicted in Fig. 2(b). The thickness and shear modulus of the shell is t and μ_s, respectively. In this case, the boundary conditions become: in the far field, $\epsilon_{rr}^{\infty} = 0$; at $r = R_t, \sigma_{rr}^s = 2\gamma/R_t, \sigma_{r\phi}^s = 0$, where superscript "$s$" stands for shell. In addition, stresses and displacements should be continuous across the shell–matrix interface, i.e., at $r = R_t + t$, $\sigma_{rr}^s = \sigma_{rr}^m$; $\sigma_{r\phi}^s = \sigma_{r\phi}^m$; $U_r^s = U_r^m$; $U_\phi^s = U_\phi^m$, where superscript "m" indicates the matrix. Assume both the shell and the matrix are incompressible materials, i.e., $\nu = 0.5$, solving this boundary value problem gives the following radius of crater after demolding:

$$R_0 = R_t\left\{1 - \frac{\eta(1+\beta)^3}{2\left[(1-\alpha) + \alpha(1+\beta)^3\right]}\right\} \tag{9}$$

where $\alpha = \mu_s/\mu_m$ is the normalized shell modulus and $\beta = t/R_t$ is the normalized shell thickness. It is obvious that Eq. (9) will decay to Eq. (8) when $\alpha = 1$or $\beta = 0$, i.e., when there is effectively no shell. The conclusion that ΔR is proportional to η is also true for Eq. (9).

2.2. Nonlinear elasticity solutions for Stage 0

According to Eq. (8), if η is 2, R_0 should be zero, indicating that the crater would disappear due to large surface tension. Such large deformation violates the small deformation assumption in linear elasticity. In fact, the spherical symmetry of the two cavities in Fig. 2 dictates that the solution for this problem should be independent of ϕ, which means that the spherical cavity will deform to another spherical shape. Under such premise, nonlinear elasticity solutions may be deduced. First, consider a spherical cavity with initial inner radius R_t (Fig. 2(a)) and an arbitrary radius R ($R \geq R_t$) in the reference configuration. When subjected to surface tension (i.e., Stage 0), it deforms to another cavity with inner radius R_0 and the radius R deforms to r ($r \geq R_0$) in the current configuration. Hence the hoop stretch is defined as $\lambda_\phi(R) = r/R$. The incompressibility of the polymer requires a constant volume of the shell confined by R_t and R, i.e.,

$$R^3 - R_t^3 = r^3 - R_0^3. \tag{10}$$

Due to spherical symmetry, the material is under a triaxial stress state $(\sigma_{rr}, \sigma_{\phi\phi}, \sigma_{\phi\phi})$. If incompressibility is considered, superposing a hydrostatic stress $(-\sigma_{rr}, -\sigma_{rr}, -\sigma_{rr})$ on the material will not change the state of deformation. Therefore, the stress state of the material becomes $(0, \sigma_{\phi\phi} - \sigma_{rr}, \sigma_{\phi\phi} - \sigma_{rr})$. The constitutive law for incompressible Neo-Hookean materials in this equibiaxial stress state can be rewritten as

$$\sigma_{\phi\phi} - \sigma_{rr} = \mu_m\left(\lambda_\phi^2 - \lambda_\phi^{-4}\right). \tag{11}$$

The nontrivial equilibrium equation of this problem is

$$\frac{d\sigma_{rr}(r)}{dr} + 2\frac{\sigma_{rr} - \sigma_{\phi\phi}}{r} = 0. \tag{12}$$

Plugging Eq. (11) into Eq. (12), and integrating Eq. (12) from $r = R_0$ to $r = \infty$ yields

$$\sigma_{rr}|_{r=\infty} - \sigma_{rr}|_{r=R_0} = \mu_m \left[\frac{5}{2} - 2\frac{R_t}{R_0} - \frac{1}{2}\left(\frac{R_t}{R_0}\right)^4 \right]. \tag{13}$$

The right hand side is a well-established function group to characterize the large deformation of hyperelastic materials [41], while the left hand side is only associated with boundary conditions in current configuration. Substituting $\sigma_{rr}|_{r=\infty} = 0$, $\sigma_{rr}|_{r=R_0} = 2\gamma/R_0$ gives an equation relating R_0 to R_t:

$$\frac{\gamma}{\mu_m R_t} = 1 - \frac{5}{4}\left(\frac{R_0}{R_t}\right) + \frac{1}{4}\left(\frac{R_t}{R_0}\right)^3. \tag{14}$$

Numerically solving Eq. (14) can yield R_0 as a function of R_t.

When a reinforcing shell is considered (Fig. 2(b)), this problem can be solved by adding the continuity conditions at the shell–matrix interface in current configuration, i.e. at $r = r_0$: $\sigma^s_{rr} = \sigma^m_{rr}$; $\sigma^s_{r\phi} = \sigma^m_{r\phi}$; $\lambda^s_\phi = \lambda^m_\phi$. After derivation (see Appendix A), the analytical relation between R_0 and R_t is given by

$$\frac{\gamma}{\mu_m R_t} = \alpha - \frac{5}{4}\frac{R_0}{R_t} + \frac{\alpha}{4}\left(\frac{R_t}{R_0}\right)^3 + (1-\alpha)\left[\frac{(1+\beta)R_0}{r_0} + \frac{1}{4}\frac{R_0}{R_t}\left(\frac{(1+\beta)R_t}{r_0}\right)^4 \right] \tag{15}$$

where $\alpha = \mu_s/\mu_m$ and $\beta = t/R_t$ are as defined before. Similarly, Eq. (15) will decay to Eq. (14) when $\alpha = 1$or $\beta = 0$ if we note that $r_0 = R_0$ when $\beta = 0$. Theoretical results for both linear and nonlinear elasticity will be presented in Section 3.

2.3. Finite element modeling

We performed FEM using a commercial package ABAQUS/standard 6.13. To simulate curvature-dependent surface tension, we implemented a four-noded isoparametric quadrilateral user-element subroutine (UEL) [42] in all following FEM jobs. Considering the axisymmetry of the problem, in 2-D space, a quarter of a small spherical cavity with radius $R_t$was built on the surface of a large polymer matrix with lateral size L_0 ($L_0 > 10R_t$) (Fig. 3(a)). The left and bottom surfaces are modeled as symmetric planes. In accordance with theoretical analysis, we used nearly incompressible Neo-Hookean material, i.e., $\nu = 0.499$, throughout the simulation. To model large deformation in FEM, nonlinear geometry (NLGEOM) is always on. We first simulated hemi-spherical cavity without reinforcing shell. Detailed procedures for Stages 0 through 2 are described as follows:

Stage 0 (demolding): Apply uniform normal traction $\kappa\gamma$ to the inner surface of the crater to simulate the demolding process. The hemi-spherical crater deforms from initial radius R_t to R_0. The volume of the crater at the end of Stage 0 is $V_0 = 2/3\pi R_0^3$. This step is realized merely by applying the UEL.

Stage 1 (loading): Apply a compressive load of $\epsilon_0 = 0.5$ on the top surface of the specimen. During compression, traction on the crater due to surface tension is still activated but varies at each incremental step with the updated local curvature. This step is completed by applying the UEL and a compressive load of $\epsilon_0 = 0.5$. At the end of this stage, the crater deforms to a shallow dome of volume V_1 which can be calculated via exported nodal coordinates of the inner surface of the crater.

Stage 2 (unloading): Remove the remote compressive load ϵ_0 and apply a positive normal traction with the amplitude of $-\Delta P = P_1 - P_2$ in addition to $\kappa\gamma$ to the surface of the crater. The pressure drop $-\Delta P$ has to be calculated by combining the ideal gas relation and Eq. (15) (see Appendix A). This step is finished by deactivating ϵ_0 and simultaneously applying UEL and $-\Delta P$. At the end of Stage 2, the crater volume V_2 can be obtained.

In fact, Stage 2 FEM is not necessary because $-\Delta P$ can be obtained analytically (see Appendix A) once V_1 is obtained by Stage 1 FEM. Therefore, Stage 2 FEM serves as a validation for the nonlinear elasticity theory.

Boundary conditions for those three stages are illustrated in Fig. 3(b)–(d). The contours plot the magnitude of normalized displacement with constant $\eta = 1$ in all stages. The shape of the crater before demolding is highlighted by the red dashed curve in Fig. 3(b) and (d). After demolding, the profile of the crater is given in Fig. 3(b) and is also drawn as the black dashed curve in Fig. 3(d). Fig. 3(c) shows that after $\epsilon_0 = 0.5$ is applied, the crater is compressed to a very shallow dome and the arrows inside the cavity indicate the nonuniform normal traction (i.e. surface tension) arising from nonuniform local curvature.

Such three-stage FEM procedure can also be applied to quantify the effects of a reinforcing shell by simply modifying the geometry and material properties of the elements near the cavity. Effects of stiffness and thickness of the reinforcing shell will be discussed in Section 3.

3. Results

3.1. Crater volume at the end of Stage 0

Regarding the demolding process (Stage 0), linear elasticity analysis in Section 2.1 concludes that when there is no reinforcing shell, the change of the crater radius (ΔR) is linearly proportional to the elasto-capillary number (η). When a reinforcing shell is introduced, crater contraction can be suppressed and the radius after demolding is given by Eq. (9). To reveal the effects of shell stiffness (α) and thickness (β), we consolidate the surface tension effect by normalizing $\Delta R/R_t$ by $-\eta/2$ and plot the linear elasticity results in Fig. 4(a) and (b) where the red horizontal lines represent unreinforced craters. It is manifest that for a given η, increasing α and β will both impede the radius shrinkage due to surface tension. Specifically, $\alpha = 30$ and $\beta = 1$ are obtained from a reported experiment where $\mu_m = 52$ kPa, $\mu_s = 1.6$ MPa, and $t = R_t = 0.5$ μm [28]. Fig. 4(a) suggests that when $\alpha = 30$ (green curve), a small value of β, say $\beta = 0.1$, will significantly resist the crater from shrinking. When $\beta = 1$ (green curve), Fig. 4(b) indicates that such a thick shell will only need $\alpha = 10$ to effectively protect the cavity from collapsing.

In contrary to linear elasticity solutions, radius change predicted by nonlinear analysis in Section 2.2 is no longer proportional to η. Analytical and FEM results of radius change as a function of η, α and β are presented in Fig. 4(c) and (d). While our nonlinear analysis fully agrees with the FEM results, the linear theory is only valid up to about $\eta = 0.5$. When η is beyond 0.5, the linear theory would greatly overestimate the radius change. For example, the linear theory predicts that the unreinforced crater should disappear when $\eta = 2$ whereas the nonlinear analysis only yields $\Delta R/R_t = -0.47$. For craters of $r \sim 0.5$ μm on the surface of 40:1 PDMS [28], $\eta = 0.769$, which should be modeled by the nonlinear theory. When $\alpha = 30$ and $\beta = 1$ (green curves in Fig. 4(c) and (d)), the radius shrinkage is almost negligible even at very large η.

3.2. Crater volume at the end of Stage 1

Section 3.1 quantified the effect of surface tension for unreinforced and reinforced craters during Stage 0. To generate suction force, the crater must be compressed to squeeze out the air, which is represented by Stage 1. Intuitively, larger volume loss during compression is preferred because more air can be driven out.

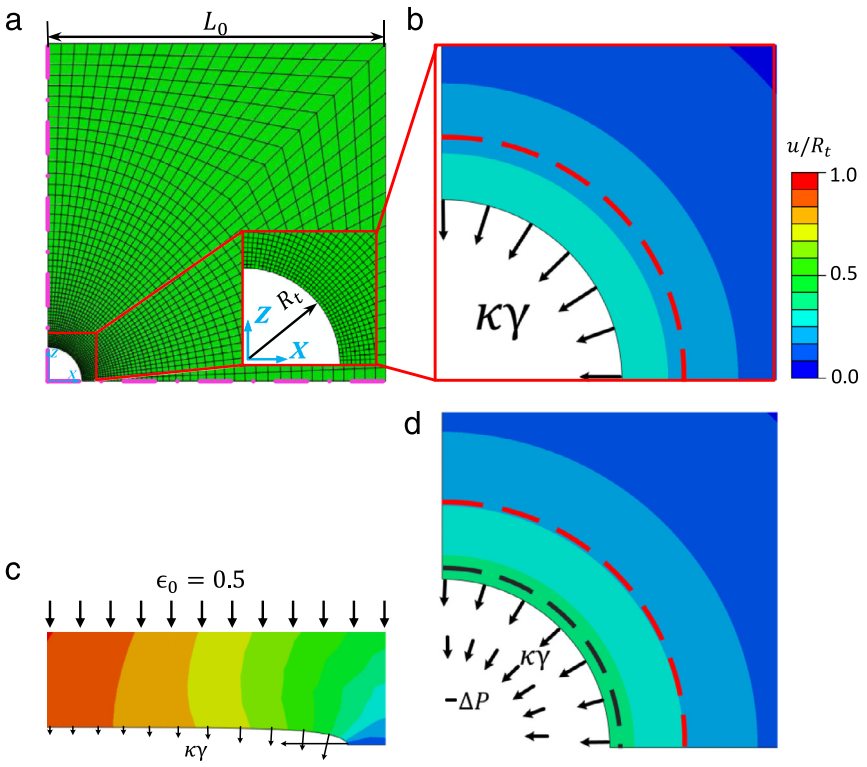

Fig. 3. (a) FEM mesh of an axisymmetric crater model with a magnified view of the refined mesh near the crater. (b)–(d) Contour plots of normalized total displacement with $\eta = 1$ at (b) State 0 where initial crater boundary is marked as red dashed curve; (c) State 1 with a preload of $\epsilon_0 = 0.5$; (d) State 2 where initial and State 0 crater shapes are represented by red and black dashed curves, respectively. (For interpretation of the references to color in this figure legend, the reader is referred to the web version of this article.)

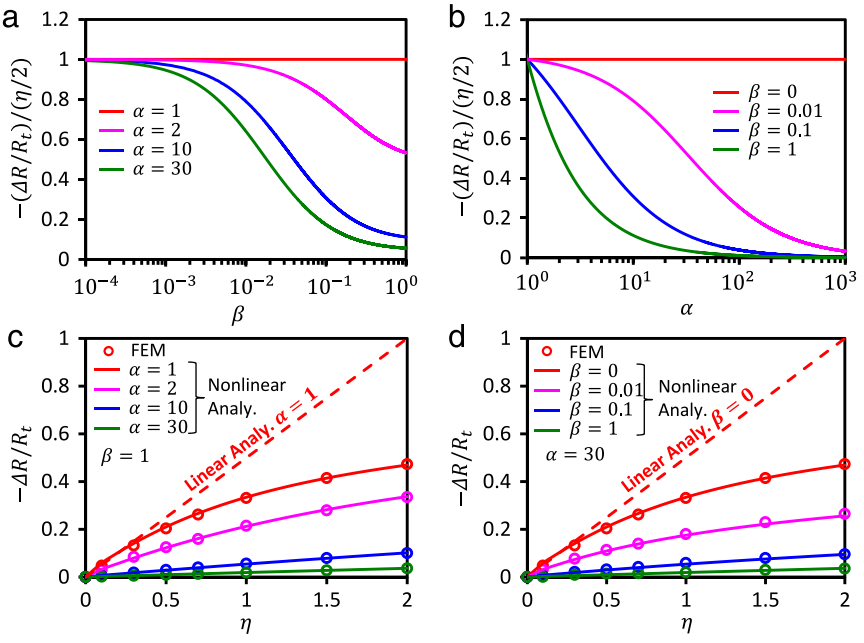

Fig. 4. Change of crater radius during Stage 0. (a)–(b) Linear elasticity results for different α and β. $\alpha = 1$ or $\beta = 0$ indicates unreinforced craters. Note that radius change is proportional to η. (c)–(d) Comparison among linear and nonlinear analytical results and FEM results for different α, β, and η. (For interpretation of the references to color in this figure legend, the reader is referred to the web version of this article.)

However, will the reinforcing shell, though plays an important role in protecting the crater shape, also resist the deformation during compression?

During Stage 1, compressive load ϵ_0 is applied remotely. We first examined the effects of surface tension on unreinforced craters ($\alpha = 1$ or $\beta = 0$). FEM results of V_1/V_t as a function of ϵ_0 are plotted for four different $\eta = 0, 0.5, 1, 2$ in Fig. 5(a). Note that when $\epsilon_0 = 0$, V_1 is the same as the crater volume at the end of Stage 0, i.e., $V_1|_{\epsilon_0=0} = V_0$. The red markers plot the results for $\eta = 0$. V_1 decreases as ϵ_0 increases and it goes to zero when ϵ_0 reaches 0.5, at which point the crater surface fully touches the flat plate and air inside the crater has been completely squeezed out.

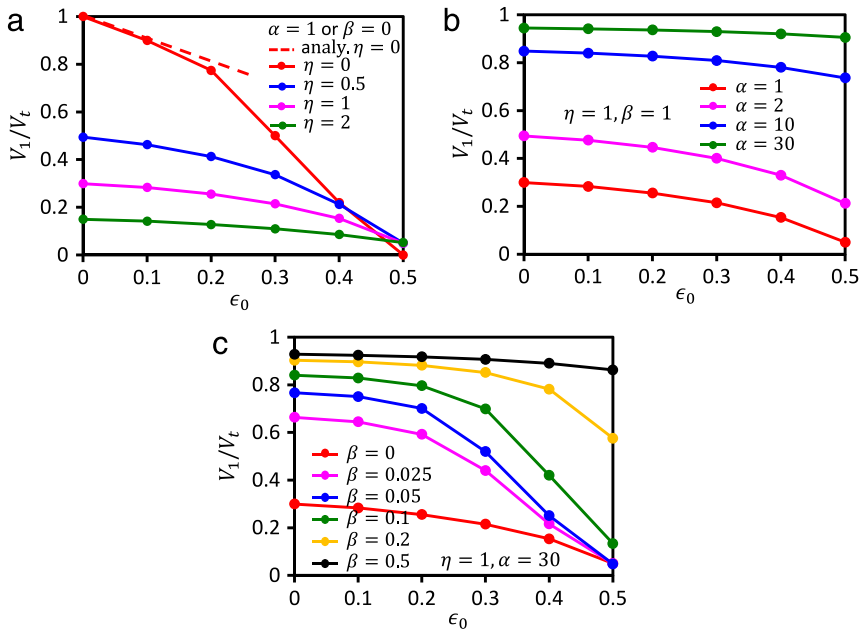

Fig. 5. Volume of the compressed crater V_1 normalized by $V_t = 2\pi R_t^3/3$ as a function of preload ϵ_0: (a) Unreinforced crater with $\beta = 0$, $\eta = 0, 0.5, 1, 2$; (b) Reinforced crater with $\eta = 1$, $\beta = 1$, $\alpha = 1, 2, 10, 30$; (c) Reinforced crater with $\eta = 1$, $\alpha = 30$, $\beta = 0, 0.025, 0.05, 0.1, 0.2, 0.5$. (For interpretation of the references to color in this figure legend, the reader is referred to the web version of this article.)

The red dashed curve is obtained from an analytical solution based on Eshelby formulism [36], which is only valid for small strains. When surface tension is taken into account, the starting values of V_1 are significantly smaller than V_t due to the volume loss at Stage 0. V_1 also decays slower than no surface tension case and almost reaches the same values at $\epsilon_0 = 0.5$ for three different $\eta = 0.5, 1, 2$, i.e., $V_1/V_t|_{\epsilon_0=0.5} \sim 0.08$. The reason it is more difficult for V_1 to vanish under nonzero η is that surface tension penalizes large curvature near the rim of the crater.

Effects of reinforcing shell are illustrated by fixing $\eta = 1$ and varying α and β. The stiffness effect is presented in Fig. 5(b) with $\eta = 1$, $\beta = 1$ and $\alpha = 1, 2, 10, 30$. It clearly shows that $\alpha = 10$ (blue) and 30 (green) not only protect the crater shape during Stage 0, but also resist crater compression during Stage 1. Such a limited volume change during compression is not favorable for suction generation. In comparison, smaller α affords larger volume change during Stage 1. However, small α also yields small V_0, which leads to a tradeoff. The thickness effect is illustrated in Fig. 5(c) with $\eta = 1$, $\alpha = 30$ and $\beta = 0, 0.025, 0.05, 0.1, 0.2, 0.5$. Encouragingly, we find that thin shells with $\beta = 0.025, 0.05, 0.1$ can protect the crater shape during demolding (i.e. large V_0) without imposing too much constraints during compression (i.e. small V_1), which have a potential in generating high pressure drop according to Eq. (3) (see movie in Supplementary Information).

3.3. Pressure drop and suction force at the end of Stage 2

When unloaded, crater springs back. At equilibrium, aside from the surface tension induced normal traction, the crater is also subjected to a negative pressure, $-\Delta P$. Therefore, ambient pressure is taken into account by introducing a new dimensionless parameter, $\delta = \mu_m/P_0$. Following the FEM procedure for Stage 2 described in Section 2.3, we can obtain V_2 after unloading. Plugging V_1 and V_2 in Eqs. (3) and (4), we would be able to obtain the pressure drop and the suction force, respectively. We can first investigate surface tension effect for unreinforced craters. Results are plotted in Fig. 6(a) with $\delta = 1$, $\alpha = 1$ and $\eta = 0, 0.5, 1, 2$. All scenarios show that pressure drop monotonically increases with ϵ_0. When $\eta = 0$, vacuum is achieved at Stage 2 when $\epsilon_0 = 0.5$, hence $-\Delta P/P_0 = 1$. When η increases, the pressure drop reduces, which clearly states that surface tension has a negative effect on pressure drop. The reason is two folds. Eq. (3) suggests that large pressure drop comes from large V_2 and small V_1. According to our three-stage analysis, we know that large V_2 relies on large V_0. Surface tension shrinks V_0 hence limits V_2. The second effect is on V_1. As mentioned in Fig. 5(a), surface tension resists compression, hence preventing the specimen from achieving small V_1.

By fixing $\eta = 1$, we can examine the effect of the stiffness of the polymer matrix on suction generation. The pressure drop for three different $\delta = 0.5, 1, 10$, i.e., $\mu_m \sim$50 kPa, 100 kPa, 1 MPa which are close to the moduli of commonly used PDMS, are plotted in Fig. 6(b). The difference between the three specimens is very small because a narrow range of δ is studied here. Thereafter, we can study the effect of reinforcing shell by simply fixing $\delta = 1$. Fig. 6(c) and (d) plot the pressure drop and the suction force for $\eta = 1$, $\delta = 1$, $\alpha = 30$ and $\beta = 0, 0.025, 0.05, 0.1, 0.2, 0.5$. The suction force F_S is normalized by $F_t = P_0 A_t$, where $A_t = \pi R_t^2$ is the projected area of the hemi-spherical dome of the molding template. Both pressure drop and suction force show non-monotonic dependence on β at $\epsilon_0 = 0.5$. They first increase as β increases and then drop after β goes beyond a certain value. This agrees with the prediction we made in Fig. 5(c) that $\beta = 0.025, 0.05, 0.1$ should yield better suction because they may sustain large V_0 after demolding and are capable of reaching small V_1 after compression. An interesting observation when comparing Fig. 6(c) and 6d is that large pressure drop does not necessarily lead to large suction force because A_2 also contributes to F_s. For example, the red curve ($\beta = 0$) has large pressure drop at $\epsilon_0 = 0.5$ in Fig. 6(c) but the generated suction force is low in Fig. 6(d). This is because the A_2 is small due to the volume loss during Stage 0.

To offer a comprehensive understanding of the effects of α and β, more FEM simulations within the parameter space $\alpha \in (0, 100)$ and $\beta \in (0, 0.5)$ are conducted with fixed $\eta = 1$ and $\delta = 1$. Contour plots of pressure drop and suction force for different combinations of α and β are shown in Fig. 6(e) and (f), respectively. Both $-\Delta P$ and F_s show non-monotonic dependence on α and β. Both figures suggest that large α and large β, i.e., thick and stiff shells, are not preferred. This is because although they

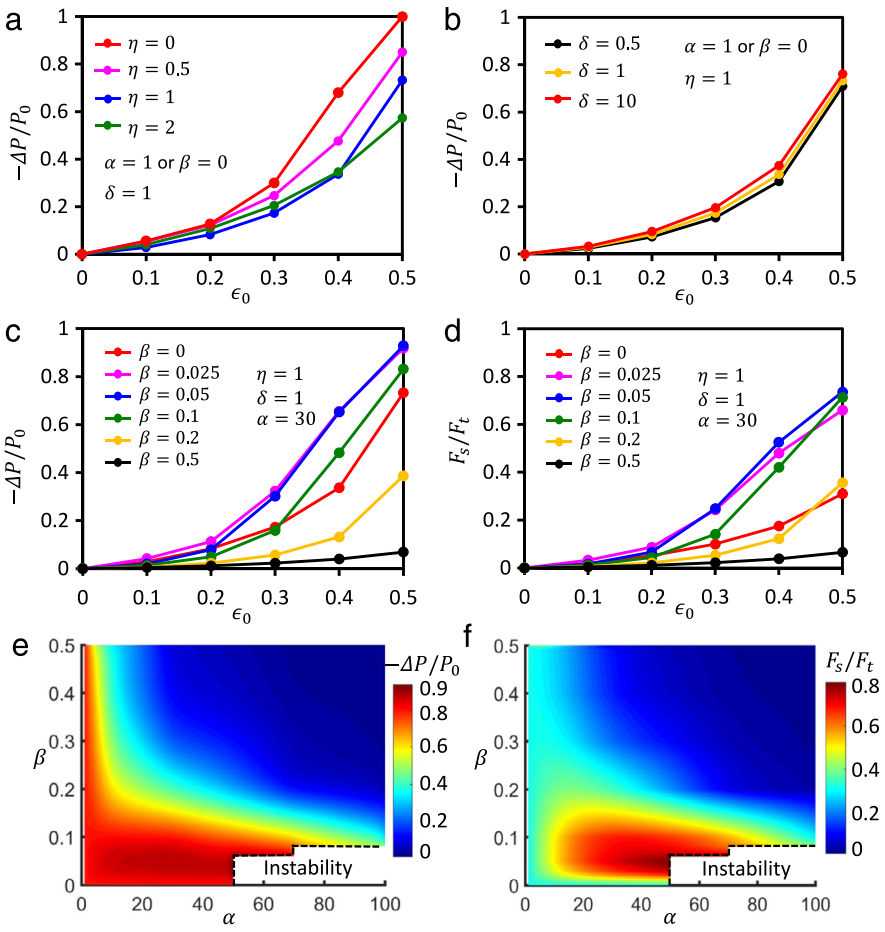

Fig. 6. (a)–(c) Normalized pressure drop as a function of ϵ_0 with (a) $\beta = 0, \delta = 1, \eta = 0, 0.5, 1, 2$; (b)$\eta = 1, \beta = 1, \delta = 0.5, 1, 10$; (c) $\eta = 1, \delta = 1, \alpha = 30, \beta = 0, 0.025, 0.05, 0.1, 0.2, 0.5$. (d) Normalized suction forces correspond to (c). (e)–(f) Contour plots of (e) normalized pressure drop and (f) normalized suction force as functions of α and β with $\eta = 1, \delta = 1, \epsilon_0 = 0.5$.

can help sustain crater shape during demolding, they also greatly resist crater compression during compression. Small α and small β does cannot offer large F_s either because they are not effective in protecting the crater shape during demolding. Therefore the optimal choice of α and β for large F_s lies in the domain $\alpha \in (20, 50)$ and $\beta \in (0.025, 0.15)$ as shown in Fig. 6(f). To quantify the suction enhancement by the reinforcing shell, we can compare the suction force generated by an optimally reinforced specimen (e.g. $\alpha = 50, \beta = 0.05$) and an unreinforced specimen ($\alpha = 1$). According to Fig. 6(f), the amplification factor can be determined to be 0.80/0.31=2.58. When α is large and β is small, some results are unattainable due to surface instabilities of the crater [36].

4. Conclusions

Suction forces generated by macroscopic craters depend on crater geometry, material properties, and applied preload. As craters miniaturize, surface tension can play a significant role especially when the micro- or even nano-craters are engineered on soft materials. In this paper, we have obtained analytical solutions for the demolding process. By implementing a user-element subroutine, we have developed a three-stage FEM process to quantify the effects of surface tension on suction forces. We found that overall, surface tension is detrimental to suction forces because it shrinks crater volume after demolding and resists full closure of crater during compression. We propose that a stiff reinforcing shell can be added to prevent the crater from contraction during demolding. However, the reinforcing shell cannot be too stiff or too thick because it will then prevent crater from collapsing during compression. Extensive simulations for various combinations of shell thickness and stiffness have revealed the optimal parametric choices. We also noticed that large pressure drop does not necessarily lead to large suction force because suction force is also dependent on the projected area after unloading. This is why adding the reinforcing shell can enhance the suction force against surface tension.

Acknowledgments

This work is supported by the NSF CMMI award under Grant No. 1301335 and the ONR YIP award under Grant No. N00014-16-1-2044. The authors are very grateful to Dr. David L. Henann in Brown University for sharing the ABAQUS user subroutine for surface tension simulation.

Appendix A

A.1. Nonlinear elasticity solutions for Stage 0 with reinforcing shell

When a reinforcing shell is considered (Fig. 2(b)), let us assume the shell–matrix interface is at $r = r_0$ at the end of Stage 0, which is referred as the current configuration. The continuity conditions at the shell–matrix interface are at $r = r_0$: $\sigma^s_{rr} = \sigma^m_{rr}$; $\sigma^s_{r\phi} = \sigma^m_{r\phi}$; $\lambda^s_\phi = \lambda^m_\phi$. For the matrix, solving Eq. (12) gives

$$\sigma^m_{rr}|_{r=\infty} - \sigma^m_{rr}|_{r=r_0} = \mu_m \left[\frac{5}{2} - 2\frac{R_t + t}{r_0} - \frac{1}{2}\left(\frac{R_t + t}{r_0}\right)^4 \right]. \quad \text{(A.1)}$$

For the reinforcing shell, similarly we have

$$\sigma_{rr}^{s}|_{r=r_0} - \sigma_{rr}^{s}|_{r=R_0} = \mu_s \left\{ 2\left(\frac{R_t+t}{r_0} - \frac{R_t}{R_0}\right) + \frac{1}{2}\left[\left(\frac{R_t+t}{r_0}\right)^4 - \left(\frac{R_t}{R_0}\right)^4\right]\right\}. \tag{A.2}$$

Adding Eqs. (A.1) and (A.2) yields

$$\begin{aligned}\sigma_{rr}^{m}|_{r=\infty} - \sigma_{rr}^{s}|_{r=R_0} &= \mu_m\left[\frac{5}{2} - 2\frac{R_t+t}{r_0} - \frac{1}{2}\left(\frac{R_t+t}{r_0}\right)^4\right] \\ &+ \mu_s\left\{2\left(\frac{R_t+t}{r_0} - \frac{R_t}{R_0}\right) \right. \\ &\left. + \frac{1}{2}\left[\left(\frac{R_t+t}{r_0}\right)^4 - \left(\frac{R_t}{R_0}\right)^4\right]\right\}.\end{aligned} \tag{A.3}$$

Note that the left hand side of Eq. (A.3) is only associated with the boundary conditions of this problem which are $\sigma_{rr}^{m}|_{r=\infty} = 0$ and $\sigma_{rr}^{s}|_{r=R_0} = 2\gamma/R_0$. Rearranging Eq. (A.3) leads to Eq. (15). Volume incompressibility of the reinforcing shell requires

$$(R_t+t)^3 - R_t^3 = r_0^3 - R_0^3. \tag{A.4}$$

Numerically solving Eqs. (A.3) and (A.4), we can get r_0 and R_0.

A.2. Pressure drop $-\Delta P$ analyzed by nonlinear elasticity

If we consider the following two facts: (1) spherical symmetry of the problem; (2) no instability happens during loading or unloading, the hemi-spherical crater should spring back to a new hemi-spherical crater with radius R_2 after unloading, i.e., at the end of Stage 2. Let us assume at the end of Stage 2, the shell–matrix interface is at $r = r_2$ in current configuration. It can be readily found that

$$\begin{aligned}\sigma_{rr}^{m}|_{r=\infty} - \sigma_{rr}^{s}|_{r=R_2} &= \mu_m\left[\frac{5}{2} - 2\frac{R_t+t}{r_2} - \frac{1}{2}\left(\frac{R_t+t}{r_2}\right)^4\right] \\ &+ \mu_s\left\{2\left(\frac{R_t+t}{r_2} - \frac{R_t}{R_2}\right) \right. \\ &\left. + \frac{1}{2}\left[\left(\frac{R_t+t}{r_2}\right)^4 - \left(\frac{R_t}{R_2}\right)^4\right]\right\}.\end{aligned} \tag{A.5}$$

Also, volume incompressibility of the reinforcing shell also requires

$$(R_t+t)^3 - R_t^3 = r_2^3 - R_2^3. \tag{A.6}$$

The boundary condition at State 2 (Fig. 1(d)) now becomes:

$$\begin{aligned}\sigma_{rr}^{m}|_{r=\infty} &= 0 \\ \sigma_{rr}^{s}|_{r=R_2} &= \frac{2\gamma}{R_2} + (-\Delta P)\end{aligned} \tag{A.7}$$

where $-\Delta P = P_1 - P_2 = P_0 - P_2$.

Invoke the ideal gas relation that $P_1V_1 = P_2V_2$ and $V_2 = 2/3\pi R_2^3$, the boundary conditions can be rewritten as

$$\begin{aligned}\sigma_{rr}^{m}|_{r=\infty} &= 0 \\ \sigma_{rr}^{s}|_{r=R_2} &= \frac{2\gamma}{R_2} + P_0\left(1 - \frac{3V_1}{2\pi R_2^3}\right)\end{aligned} \tag{A.8}$$

where V_1 has to be obtained by Stage 1 FEM.

Numerically solving Eqs. (A.5) and (A.6), we can get r_2 and R_2. This nonlinear elasticity method is verified by FEM. R_2 obtained by this derivation is found to be identical with that computed by Stage 2 FEM as described in Section 2.3. Therefore, results presented in Fig. 6 are based on nonlinear elasticity method.

Note that setting $\mu_s = \mu_m$ or $t = 0$ in Eqs. (A.3) and (A.5) will lead to unreinforced craters.

Appendix B. Supplementary data

Supplementary material related to this article can be found online at http://dx.doi.org/10.1016/j.eml.2017.07.004.

References

[1] C. Menon, M. Murphy, M. Sitti, Gecko inspired surface climbing robots, in: IEEE International Conference on Proc. Robotics and Biomimetics, ROBIO 2004, IEEE, 2004, pp. 431–436.

[2] H. Kim, D. Kim, H. Yang, K. Lee, K. Seo, D. Chang, J. Kim, Development of a wall-climbing robot using a tracked wheel mechanism, J. Mech. Sci. Technol. 22 (8) (2008) 1490–1498.

[3] M.J. Spenko, G.C. Haynes, J.A. Saunders, M.R. Cutkosky, A.A. Rizzi, R.J. Full, D.E. Koditschek, Biologically inspired climbing with a hexapedal robot, J. Field Robot. 25 (4–5) (2008) 223–242.

[4] W.-Y. Chang, Y. Wu, Y.-C. Chung, Facile fabrication of ordered nanostructures from protruding nanoballs to recessional nanosuckers via solvent treatment on covered nanosphere assembled monolayers, Nano Lett. 14 (3) (2014) 1546–1550.

[5] H. Lee, D.S. Um, Y. Lee, S. Lim, H.j. Kim, H. Ko, Octopus-inspired smart adhesive pads for transfer printing of semiconducting nanomembranes, Adv. Mater. 28 (34) (2016) 7457–7465.

[6] M.K. Kwak, H.E. Jeong, K.Y. Suh, Rational design and enhanced biocompatibility of a dry adhesive medical skin patch, Adv. Mater. 23 (34) (2011) 3949–3953.

[7] W.G. Bae, D. Kim, M.K. Kwak, L. Ha, S.M. Kang, K.Y. Suh, Enhanced skin adhesive patch with modulus-tunable composite micropillars, Adv. Healthc. Mater. 2 (1) (2013) 109–113.

[8] M.K. Choi, O.K. Park, C. Choi, S. Qiao, R. Ghaffari, J. Kim, D.J. Lee, M. Kim, W. Hyun, S.J. Kim, H.J. Hwang, S.-H. Kwon, T. Hyeon, N. Lu, D.-H. Kim, Cephalopod-inspired miniaturized suction cups for smart medical skin, Adv. Healthc. Mater. 5 (1) (2015) 80–87.

[9] Y.-C. Chen, H. Yang, Octopus-inspired assembly of nanosucker arrays for dry/wet adhesion, ACS Nano (2017).

[10] A. Mahdavi, L. Ferreira, C. Sundback, J.W. Nichol, E.P. Chan, D.J. Carter, C.J. Bettinger, S. Patanavanich, L. Chignozha, E. Ben-Joseph, A biodegradable and biocompatible gecko-inspired tissue adhesive, Proc. Natl. Acad. Sci. 105 (7) (2008) 2307–2312.

[11] K. Autumn, Y.A. Liang, S.T. Hsieh, W. Zesch, W.P. Chan, T.W. Kenny, R. Fearing, R.J. Full, Adhesive force of a single gecko foot-hair, Nature 405 (6787) (2000) 681–685.

[12] E. Arzt, S. Gorb, R. Spolenak, From micro to nano contacts in biological attachment devices, Proc. Natl. Acad. Sci. USA 100 (19) (2003) 10603–10606.

[13] R. Spolenak, S. Gorb, E. Arzt, Adhesion design maps for bio-inspired attachment systems, Acta Biomater. 1 (1) (2005) 5–13.

[14] H. Yao, H. Gao, Mechanics of robust and releasable adhesion in biology: Bottom-up designed hierarchical structures of gecko, J. Mech. Phys. Solids 54 (6) (2006) 1120–1146.

[15] E.P. Chan, C. Greiner, E. Arzt, A.J. Crosby, Designing model systems for enhanced adhesion, MRS Bull. 32 (6) (2007) 496–503.

[16] H. Lee, B.P. Lee, P.B. Messersmith, A reversible wet/dry adhesive inspired by mussels and geckos, Nature 448 (7151) (2007) 338–341.

[17] R. Sahay, H.Y. Low, A. Baji, S. Foong, K.L. Wood, A state-of-the-art review and analysis on the design of dry adhesion materials for applications such as climbing micro-robots, RSC Adv. 5 (63) (2015) 50821–50832.

[18] A.M. Smith, Negative-pressure generated by octopus suckers - a study of the tensile-strength of water in nature, J. Exp. Biol. 157 (1991) 257–271.

[19] W.M. Kier, A.M. Smith, The structure and adhesive mechanism of octopus suckers, Integr. Comp. Biol. 42 (6) (2002) 1146–1153.

[20] J. Von Byern, W. Klepal, Adhesive mechanisms in cephalopods: a review, Biofouling 22 (5) (2006) 329–338.

[21] F. Tramacere, A. Kovalev, T. Kleinteich, S.N. Gorb, B. Mazzolai, Structure and mechanical properties of Octopus vulgaris suckers, J. R. Soc. Interface 11 (91) (2014).

[22] J. Liu, K. Tanaka, L. Bao, I. Yamaura, Analytical modelling of suction cups used for window-cleaning robots, Vacuum 80 (6) (2006) 593–598.

[23] D. Ge, T. Matsuno, Y. Sun, C. Ren, Y. Tang, S. Ma, Quantitative study on the attachment and detachment of a passive suction cup, Vacuum 116 (2015) 13–20.

[24] L. Heepe, M. Varenberg, Y. Itovich, S.N. Gorb, Suction component in adhesion of mushroom-shaped microstructure, J. R. Soc. Interface 8 (57) (2011) 585–589.
[25] J. Waters, H. Gao, P. Guduru, On adhesion enhancement due to concave surface geometries, J. Adhes. 87 (3) (2011) 194–213.
[26] B. Roman, J. Bico, Elasto-capillarity: deforming an elastic structure with a liquid droplet, J. Phys.: Condens. Matter 22 (2010) 493110.
[27] J.-L. Liu, X.-Q. Feng, On elastocapillarity: A review, Acta Mech. Sinica 28 (4) (2012) 928–940.
[28] M.K. Choi, O.K. Park, C. Choi, S. Qiao, R. Ghaffari, J. Kim, D.J. Lee, M. Kim, W. Hyun, S.J. Kim, H.J. Hwang, S.H. Kwon, T. Hyeon, N. Lu, D.H. Kim, Cephalopod-inspired miniaturized suction cups for smart medical skin, Adv. Healthc. Mater. 5 (1) (2016) 80–87.
[29] S. Akerboom, J. Appel, D. Labonte, W. Federle, J. Sprakel, M. Kamperman, Enhanced adhesion of bioinspired nanopatterned elastomers via colloidal surface assembly, J. R. Soc. Interface 12 (102) (2015) 20141061.
[30] S. Baik, D.W. Kim, Y. Park, T.-J. Lee, S. Ho Bhang, C. Pang, A wet-tolerant adhesive patch inspired by protuberances in suction cups of octopi, Nature 546 (7658) (2017) 396–400.
[31] C.-Y. Hui, A. Jagota, Surface tension, surface energy, and chemical potential due to their difference, Langmuir 29 (36) (2013) 11310–11316.
[32] D.L. Henann, L. Anand, Surface tension-driven shape-recovery of micro/nanometer-scale surface features in a Pt 57.5 Ni 5.3 Cu 14.7 P 22.5 metallic glass in the supercooled liquid region: a numerical modeling capability, J. Mech. Phys. Solids 58 (11) (2010) 1947–1962.
[33] J. Huang, J. Mazzara, S. Schwendeman, M. Thouless, Self-healing of pores in PLGAs, J. Control. Release 206 (2015) 20–29.
[34] S. Wu, Calculation of interfacial tension in ploymer systems, J . Polym. Sci. C Polym. Symp. 34 (1) (1971) 19–31.
[35] R.-J. Roe, Parachor and surface tension of amorphous polymers, J. Phys. Chem. 69 (8) (1965) 2809–2810.
[36] S. Qiao, L. Wang, H. Jeong, J. Gregory, . Rodin, N. Lu, Suction effects in cratered surfaces, J. R. Soc. Interface (2017) (submitted for publication).
[37] F. Mancarella, R.W. Style, J.S. Wettlaufer, Interfacial tension and a three-phase generalized self-consistent theory of non-dilute soft composite solids, Soft Matter 12 (10) (2016) 2744–2750.
[38] R.W. Style, J.S. Wettlaufer, E.R. Dufresne, Surface tension and the mechanics of liquid inclusions in compliant solids, Soft Matter 11 (4) (2015) 672–679.
[39] F. Yang, Size-dependent effective modulus of elastic composite materials: spherical nanocavities at dilute concentrations, J. Appl. Phys. 95 (7) (2004) 3516–3520.
[40] A.I. Lur'e, Three-Dimensional Problems of the Theory of Elasticity, Interscience Publishers, 1964.
[41] J. Zhu, T. Li, S. Cai, Z. Suo, Snap-through expansion of a gas bubble in an elastomer, J. Adhes. 87 (5) (2011) 466–481.
[42] D.L. Henann, K. Bertoldi, Modeling of elasto-capillary phenomena, Soft Matter 10 (5) (2014) 709–717.